# Improved tribocorrosion behavior on bio-functionalized β-type titanium alloy by the pillar effect given by TiN reinforcements

Ihsan Çaha [a,*], Alexandra C. Alves [a], Caterina Chirico [b], Ana Maria Pinto [a,c], Sophia Tsipas [b,d], Elena Gordo [b,d], Fatih Toptan [a,e,f]

[a] CMEMS-UMinho - Center for MicroElectroMechanical Systems, Universidade do Minho, Azurém, 4800-058 Guimarães, Portugal
[b] Universidad Carlos III de Madrid, Avda. Universidad, 30, 28911 Leganés, Spain
[c] Universidade do Minho, Dept. Eng. Mecânica, Azurém, 4800-058 Guimarães, Portugal
[d] Instituto "Álvaro Alonso Barba", 30, 28911 Leganés, Madrid, Spain
[e] Department of Materials Science and Engineering, Izmir Institute of Technology, 35430 Urla, Izmir, Turkey
[f] IBTN/Euro – European Branch of the Institute of Biomaterials, Tribocorrosion and Nanomedicine, Dept. Eng. Mecânica, Universidade do Minho, Azurém, 4800-058 Guimarães, Portugal

## ARTICLE INFO

## ABSTRACT

A novel multi-functional material was developed by hard TiN particle reinforcement addition to a β-type Ti alloy, following by bio-functionalization of its surface through Ca and P rich oxide layer. Corrosion and tribocorrosion behavior of this multi-functional material was investigated in phosphate buffer solution at body temperature. Bio-functionalization drastically improved the corrosion and tribocorrosion behavior of the unreinforced and reinforced samples, where the bio-functionalized β-type titanium alloy matrix composite presented the best tribocorrosion behavior due to the load-carrying role of the hard reinforcement phase that gave a support to the functionalized surface layer.

## 1. Introduction

β-Type Ti alloys have been the focus of research among metallic based biomaterials particularly for load-bearing applications, hard tissue replacement, and fracture healing, mainly due to their two important properties [1,2]: First, they show excellent mechanical compatibility resulted from their low Young's modulus values and appropriate strength which is crucial for reducing stress shielding effect that hinders bone ingrowth [3,4]. Second, they are mostly composed of non-toxic elements, thus, expected to be a good alternative to the most widely employed Ti alloy, α + β type Ti-6Al-4V alloy, which has great concerns due to the release of harmful Al and V ions to cells and tissues [5–7]. However, recently it has been reported that β-type Ti alloys present poor wear resistance compared to Ti-6Al-4V alloy under different tribological conditions, mainly due to the low strain hardening behavior of the β phase [8–11]. The generated wear debris cause osteolysis and eventually implant failure may occur [12]. Hard coatings have been extensively proposed to overcome the poor wear resistance of Ti and its alloys [13–18]. One of the most studied hard coatings for load-bearing applications is TiN coatings due to its high hardness [19],

superior wear resistance [20], excellent corrosion resistance [21], and good biocompatibility [22]. However, their inherent brittleness and low fracture toughness are still a major concern for load-bearing applications [23,24].

Metal matrix composites (MMCs) reinforced with hard particles have been well studied in order to overcome the possible low fracture toughness of hard coatings and also to improve the wear resistance [25]. Ti and its alloys reinforced with TiN particles might potentially overcome the problems related to TiN coatings applied on monolithic metal. Romero et al. [26] studied mechanical and microstructural behavior of Ti matrix composites (TMCs) reinforced by TiN particles and reported a significant improvement in hardness not only due to load carrying effect of hard TiN particles, but also the modifications on the matrix microstructure. Similarly, mechanical and microstructural properties of spark plasma sintered Ti-6Al-4V reinforced with nano TiN particles were studied by Maja et al. [27]. The authors reported that the addition of nanosized TiN led to the transformation of α and β phases to a bimodal structure together with drastic increase of hardness and Young's modulus. Furthermore, the fracture toughness of Ti-6Al-4V alloy was improved with reinforced nano TiN particles [28]. Kundu et al. [29]

---

studied the effect of volume fraction of TiN on hardness and wear behavior of Ti-6Al-4V alloy and it was reported a direct proportional ratio between volume fraction, hardness, and wear behavior. Regarding corrosion, the main determining parameter is the formation of defects or discontinuities at the matrix/reinforcement interface, which can lead to localized corrosion or galvanic coupling [30–32]. Toptan et al. [31] studied the corrosion and tribocorrosion behavior of Ti-B$_4$C composite in 9 g/l NaCl solution and reported increased corrosion kinetics resulted from localized corrosion due to the formation of porosity around agglomerated B$_4$C particles. However, Silva et al. [33] demonstrated that the defect-free interface between matrix and reinforcement of hybrid in-situ Ti-TiB-TiN$_x$ composite did not deteriorate the corrosion behavior, but significantly improved the tribocorrosion behavior under 1 N normal load in 9 g/l NaCl solution.

While Ti and its alloys are one of the best biocompatible metallic materials, their bioinert behavior cannot lead to bone growth. Micro-arc oxidation (MAO) technique is well studied in the literature not only to improve the bioactivity of Ti and its alloys but also to improve the corrosion and tribocorrosion behavior through a formation of desired surface characteristics [34–40]. Also, the MAO treatment allows incorporating the bioactive agents such as Ca and P allowing to obtain a Ca/P ratio that similar to hydroxyapatite. As a consequence of improved surface roughness, better wettability, and bioactivity, the MAO treated β-type Ti alloys present better adhesion, proliferation, and differentiation of cells [41–45].

Poor tribocorrosion resistance and lack of bioactivity are major limiting factors for non-toxic and low Young's modulus β-type Ti alloys to be used in load-bearing biomedical applications. Therefore, the present work aimed to develop a novel multi-functional material not only to improve the tribocorrosion behavior of β-type Ti alloys, but also to improve their biological behavior. For this reason, a β-type Ti-25Nb-5Fe alloy was reinforced with hard TiN particles by powder metallurgy route, and bio-functionalized through MAO treatment with incorporation of Ca and P. The corrosion and tribocorrosion behavior was investigated in a physiological solution at body temperature.

## 2. Materials and methods

### 2.1. Materials and sample preparation

The raw material used in this study for obtaining Ti-25Nb-5Fe in wt % alloy was commercial TiH$_2$ powder (GfE, D$_{50}$ < 63 μm), Nb powder (Sat-Nano, D$_{50}$: 18 μm), and Fe powder (H.C. Starck, D$_{50}$: 5 μm). The alloy was reinforced with 5% vol. of TiN powder (Sigma-Aldrich, D$_{50}$: 1–5 μm). Mixtures of samples were prepared by wet planetary milling to improve the dispersion of powders with milling for 2 h at 150 rpm in isopropanol at a ball-powder ratio of 10:1 in weight. Then, mixtures were dried in a rotary evaporator and green compacts were pressed at 700 MPa (16 mm in diameter and about 4 mm in height), then sintered under 1450 °C for 4 h with a high vacuum (10$^{-5}$ mbar). The Ti-25Nb-5Fe alloy and its composites were labeled as Alloy and MMC, respectively. Samples were grounded with SiC papers down to 2400 mesh size and mirror-finished by using colloidal silica suspension (Buehler, 0.02 μm), following by ultrasonically cleaning in propanol and distilled water for 10 min and 5 min, respectively. Before tests, samples were held up in a desiccator for a day before starting each test.

### 2.2. Bio-functionalization by micro-arc oxidation

Mirror finished samples were subjected to MAO in an aqueous electrolyte including a mixture of 0.35 M calcium acetate monohydrate (CA, Fluka) and 0.02 M β-glycerophosphate disodium salt pentahydrate (β-GP, Alfa Aesar) in order to obtain Ca and P-rich bio-functionalized surface. The MAO treatment was performed under potentiostatic regime at 300 V by DC power supply (Agilent N5772A) under a limiting current of 2.5 A during 1 min at room temperature under 500 rpm of

magnetic stirrer conditions. A platinum foil was used as a cathode with a 7.0 cm$^2$ exposure area, and distance between Pt foil and samples (anode, with 1.5 cm$^2$ exposure area) was kept in 8 cm. After the bio-functionalization, all samples were cleaned by propanol and distilled water and dried with warm air. The MAO treated Alloy and MMC samples were labeled as MAO-Alloy and MAO-MMC, respectively.

### 2.3. Corrosion and tribocorrosion tests

Degradation behavior was investigated by corrosion and tribocorrosion tests in phosphate buffer solution (PBS; 0.2 g/l KCl, 0.24 g/l KH$_2$PO$_4$, 8 g/l NaCl, 1.44 g/l Na$_2$HPO$_4$) at body temperature (37 °C). The Corrosion behavior was studied by open circuit potential (OCP), electrochemical impedance spectroscopy (EIS), and potentiodynamic polarization measurements on 0.38 cm$^2$ exposure area in 180 ml electrolyte (adapted from ASTM: G3-89) placed using Gamry Potentiostat/ Galvanostat/ZRA (model Reference-600+). An Ag/AgCl (KCl saturated) electrode was used as a reference electrode (RE), a platinum net was used as the counter electrode (CE), and the samples were used as a working electrode (WE). EIS was performed after stabilization of samples of OCP (ΔE < 60 mV for last hour) by scanning a frequency range from 10$^5$ to 10$^{-2}$ Hz with an AC signal of 10 mV and counting 7 points per frequency decade. Afterward, the potentiodynamic polarization measurement was performed with a 0.5 mV/s scan rate, starting to scan at −0.25 V$_{OCP}$ up to 1.5 V$_{Ag/AgCl}$.

Tribocorrosion behavior was studied in a triboelectrochemical cell installed on a reciprocating tribometer (CETR-UMT-2). The tests were carried out against the alumina ball (10 mm in diameter, Ceratec) in 30 ml PBS electrolyte by using a Gamry Potentiostat/Galvanostat (model Reference-600) together with same electrodes that used in the corrosion tests. OCP was monitored before, during, and after sliding. The sliding started under 1 N of normal load, 5 mm of displacement amplitude, 1 Hz of frequency, and 30 min of sliding time.

### 2.4. Characterizations

The microstructure of the bare alloy and composite, and wear scars of counter material were analyzed by optical microscope (OM, Leica-DM2500) after etching in Kroll's reagent (%3 vol HF + %6 vol HNO$_3$ + %91 vol H$_2$O). Surface morphology of the bare (alloy and composite) samples (FEI Quanta 650), MAO treated samples, and wear tracks was analyzed by secondary electron (SE) and backscattered electron (BSE) mode of scanning electron microscopy (SEM) equipped with energy dispersive spectroscopy (EDS) for elemental analysis (FEI Nova 200). The volume fraction of each phase in the MMC sample was calculated using ImageJ 1.51j8 software. Vickers micro-hardness and macro-hardness values were studied by using Emcotest Durascan tester and Officine Galileo Mod. D200 tester, respectively, by a mean of 10 indentations performed randomly per 3 different samples with a load of 0.5 kgf (micro-hardness) and 15 kgf (macro-hardness) during 15 s. The electron backscattering diffraction (EBSD) coupled with the EDS-SEM (FEI Quanta 400) operating at 15 kV was used in order to evaluate the phase mapping, Kikuchi patterns, and crystallographic orientation of each phase in MMC sample. The MAO treated samples were embedded in a hard resin, cut with a diamond disc, ground with SiC papers up to 2400 mesh, and polished with colloidal silica suspension (Buehler, 0.02 μm) to analyze the cross-section. The phase analysis was employed by X-ray diffraction (XRD, Bruker D8 Discover diffractometer) scanning from an angle of (2θ) 20° to 80° with a 0.02°/s step size. Surface wettability was accessed by contact angle measurements through a sessile drop method using an optical tensiometer (dataphysics, OCA 15 plus). A 5 μl droplet of ultra-pure water was dropped on the surface of the samples and the contact angle was considered after 10 s at room temperature. Three different samples per group were analyzed and the drop image was recorded by using a video camera. The wear track profiles and total wear volume loss was evaluated by 3D profilometry (Profilm3D) over

three different samples.

## 3. Results

Fig. 1a and b shows SE and BSE SEM images together with an insert OM microstructure images of Ti-25Nb-5Fe alloy and its composite. As can be seen in Fig. 1a, the alloy presented single phase microstructure included pores. The MMC samples showed two well-differentiated phases, where the bright zones on SEM images correspond to the matrix, and dark one corresponding to the TiN reinforced phase with a 45.6% volume fraction. Also, the MMC samples exhibited smaller grain size and homogeneous dispersion of reinforcing phase through matrix, free from any gross defects such as porosity and cracks. Regarding hardness, the TiN reinforcement was significantly improved the Vickers macro hardness of Alloy as $449 \pm 17$ $HV_{15}$, $275 \pm 4$ $HV_{15}$, respectively. Also, the reinforced phase was presented drastically higher micro hardness values as compared to its matrix in the MMC sample by $846 \pm 65$ $HV_{0.5}$ and $421 \pm 25$ $HV_{0.5}$, respectively.

To identify each phase, EBSD analysis was performed on the MMC sample operating at 15 kV. The BSE image of both phases and its phase mapping image is given in Fig. 1c and d, respectively. The red regions correspond to the body-centered cubic (bcc) β-Ti phase as given its Kikuchi pattern and index (ICCD 00-044-1288) in Fig. 1f. The green regions presented the hexagonal close-packed (hcp) $TiN_{0.3}$ phases as identified by its Kikuchi pattern and index (ICCD 00-041-1352) in Fig. 1g. Also, the EBSD crystallographic orientation color map image is shown in Fig. 1e. Specifically, most of the areas of the matrix are green corresponding to the bcc (101) indices in the normal direction. The reinforced hcp $TiN_{0.3}$ phase indicated different crystallographic orientations in the β-Ti matrix.

The top view and cross-section images together with EDS and XRD spectra of MAO treated samples are shown in Fig. 2. As can be seen in SE and BSE SEM images, MAO-Alloy and MAO-MMC samples presented a uniform micro-porous volcano-like structure. Similar morphologies observed on the matrix and reinforcing phase of MAO-MMC samples. Regarding cross-sections, both samples presented a triplex anodic layer structure; barrier film formed at metal-anodic layer interface, inner porous layer with small pores, and outer porous layer with larger pores [35]. The average overall thickness of anodic layers for MAO-Alloy and MAO-MMC samples was the approximately 6 and 8 μm, respectively. Moreover, the anodic layer formed on both phases of MAO-MMC

samples showed the same triplex structure, where no visible differences were observed. The EDS spectra indicating the incorporation of Ca and P for both samples. The Ca/P atomic ratio was 2.65 and 2.75 for overall MAO-Alloy and overall MAO-MMC samples, respectively. Also, the Ca/P atomic ratio was 2.17 and 2.91 for Z1 and Z2, respectively, showing higher the Ca/P atomic ratio on the reinforcement phase. Nitrogen (N) was not detected by EDS most probably due to relatively high thickness of the MAO layer. Regarding XRD results, while the XRD pattern of Alloy presented fully β-Ti phase (ICCD 00-044-1288), the MMC composed of β-Ti phase (ICCD 00-044-1288) and $TiN_{0.3}$ phase (ICCD 00-041-1352) as in accordance with the EBSD results. In the case of bio-functionalized samples, in addition to their substrate peaks, both MAO treated samples presented anatase (ICCD 00-021-1272) and rutile (ICCD 01-070-7347) $TiO_2$ peaks.

The surface properties of the material are the first key affecting the biological response of a biomaterial. Being one of the most important parameter, the wettability of samples was investigated through contact angle measurements and the results are given in Fig. 2i, together with the representative optical images. Both bio-functionalized samples presented similar and drastically lower contact angle values compared to their untreated substrate. Among untreated samples, MMC showed a lower contact angle compared to Alloy.

The corrosion behavior was studied by potentiodynamic polarization measurement in PBS solution at 37 °C and the results are given in Fig. 3a. Corrosion potential ($E_{(i=0)}$) and passivation current density ($i_{pass}$) taken at 0.5 $V_{Ag/AgCl}$ were obtained from potentiodynamic polarization curves are shown in Table 1, together with recorded OCP values during last 10 min. Alloy and MMC showed similar $E_{OCP}$, $E_{(i=0)}$, and $i_{pass}$ values and a well-defined passivation plateau. Both bio-functionalized groups presented a passive region but a slight increase of current above approximately 0.75 V that may be explained by the dissolution of Ca and P on the MAO layer. Significant increase of $E_{OCP}$, $E_{(i=0)}$ and significant decrease of the $i_{pass}$ were observed from untreated groups to MAO treated groups.

Fig. 3b and c presents the EIS for untreated and bio-functionalized samples in the form of Bode diagram. At the high-frequency range, the constant values of |Z| and phase angles close to 0° were obtained for Alloy and MMC showing a typical response of the electrolyte resistance. Both untreated groups showed one time constant, and their phase angle approaching −90° in low and middle-frequency range suggesting the capacitive behavior of a compact oxide film. The MMC presented a
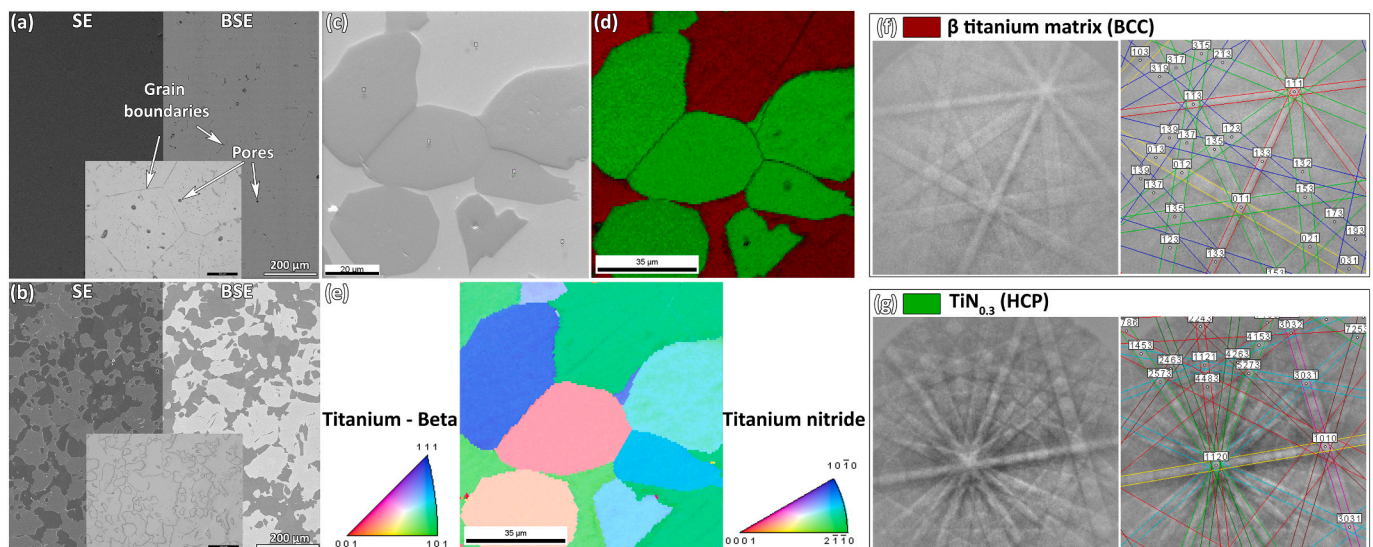


**Fig. 1.** SE and BSE SEM images together with insert OM images of microstructure of a) Alloy and b) MMC samples. The EBSD results of the MMC sample; c) BSE image of both phases, d) its phase mapping image, e) the crystallographic orientation map and the corresponding inverse pole figure of MMC sample f) Kikuchi pattern of the matrix, g) Kikuchi pattern of reinforced phase.
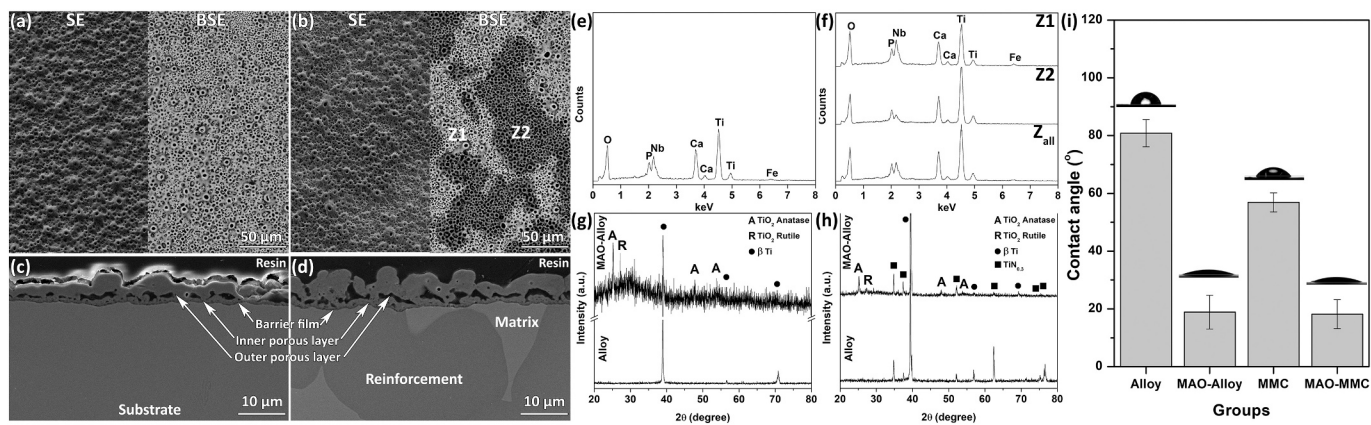
**Fig. 2.** Top view SE/BSE SEM, SE cross-section image, EDS spectra, and XRD spectra of MAO-Alloy in (a), (c), (e), and (g), and MAO-MMC in (b), (d), (f), and (h), respectively. Contact angle values and representative optical images given in (i).
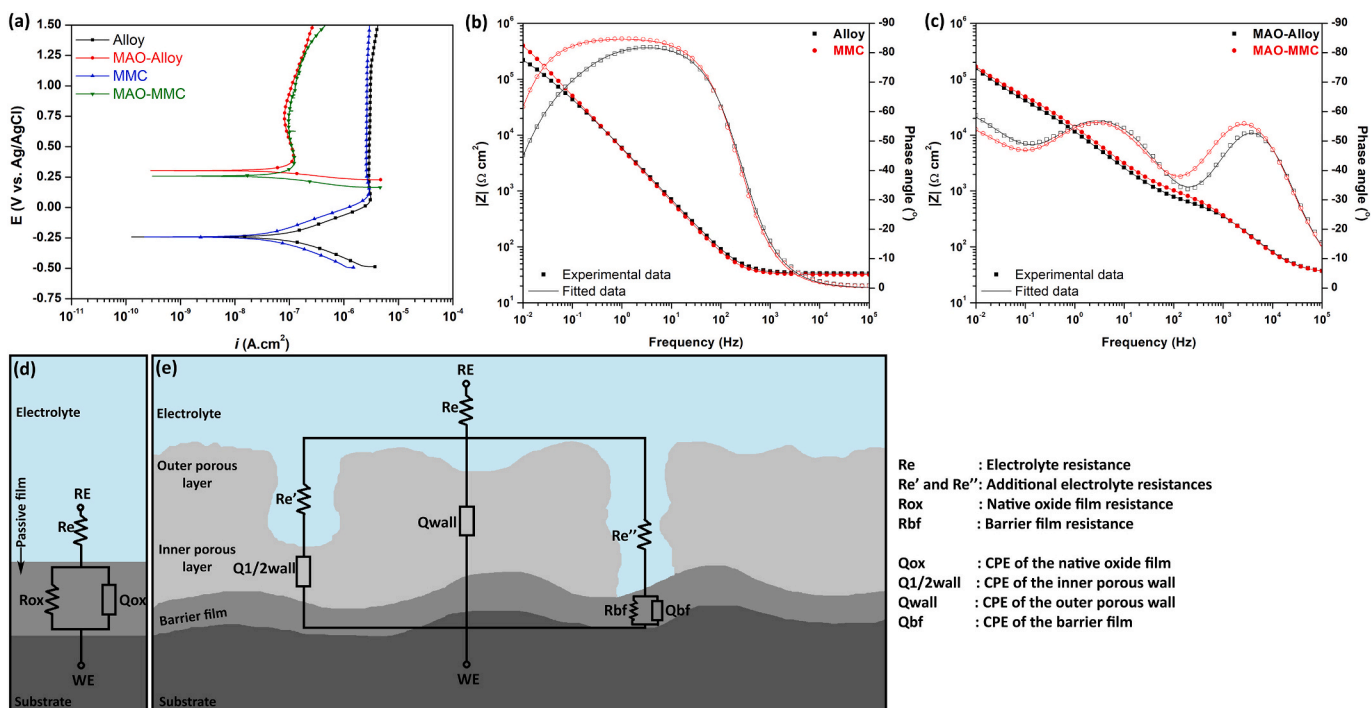


**Fig. 3.** Corrosion behavior: a) Representative potentiodynamic polarization curves of untreated and treated groups; Bode diagrams of b) Alloy and MMC, c) MAO-Alloy and MAO-MMC; EEC proposed for d) Alloy and MMC, and e MAO-Alloy and MAO-MMC. (Adapted from [58].)

**Table 1**

Corrosion potential ($E_{(i=0)}$) and passivation current density ($i_{pass}$) values obtained from potentiodynamic polarization curves.

| Groups | $E_{OCP}$ ($V_{SCE}$) | $E_{(i=0)}$ ($V_{SCE}$) | $i_{pass}$ ($\mu A \cdot cm^{-2}$) |
|---|---|---|---|
| Alloy | $-0.30 \pm 0.03$ | $-0.25 \pm 0.02$ | $2.73 \pm 0.33$ |
| MMC | $-0.29 \pm 0.04$ | $-0.25 \pm 0.04$ | $2.62 \pm 0.02$ |
| MAO-Alloy | $0.54 \pm 0.04$ | $0.28 \pm 0.03$ | $0.12 \pm 0.02$ |
| MAO-MMC | $0.50 \pm 0.10$ | $0.26 \pm 0.07$ | $0.12 \pm 0.04$ |

higher phase angle at the middle and low-frequency range and higher |Z| values at low-frequency range. Regarding the MAO-Alloy and MAO-MMC samples, both groups presented three-time constants and their phase angle approached to $-60°$ values. Both groups showed relatively similar |Z| and phase angle values. Fig. 3d and e shows the schematic representation of the electrical equivalent circuit (EEC) used for fitting

the EIS experimental data of the untreated and bio-functionalized groups, respectively. The $R_e$, $R_{ox}$, and $Q_{ox}$ are the electrolyte resistance, the resistance of natural passive oxide film, and a constant phase element (CPE), respectively, the CPE considering a non-ideal capacitance of passive oxide film. The $R_{bf}$ and $Q_{bf}$ are showing resistance and a CPE of the barrier film, respectively. Regarding the porous layer, since the thickness of corresponding layers were too high leading poor electronic conductivity, only the CPE of the outer porous layer and the inner porous layer was considered as representing the $Q_{wall}$ and $Q_{1/2wall}$, respectively. The $R_e'$ is additional resistance of the electrolyte inside the outer pores and the $R_e''$ is additional resistance of the electrolyte inside the inner pores.

The CPE showing a shift from an ideal capacitor used in EECs. The impedance of CPE is defined as: $Z_{CPE} = [Y_0(jw)^n]^{-1}$, where $-1 \leq n \leq 1$. A non-ideal capacitor may be described by a CPE if $n \cong 1$. The EEC parameters obtained from EIS experimental data for untreated and bio-

functionalized groups are given in Table 2. The quality of fitting on the proposed EECs was evaluated by the $\chi^2$ (goodness of fitting) where the proposed models showed values below $10^{-4}$.

The evolution of OCP before, during, and after sliding together with the evolution of coefficient of friction (COF) is given in Fig. 4a. Before sliding, bio-functionalized samples showed significantly higher OCP values and all samples presented stable OCP values in agreement with $E_{OCP}$ values shown in Table 1. As soon as sliding started, a sudden drop on OCP was recorded for Alloy and MMC samples due to mechanical destruction of the passive film eventually exposing the corrosive electrolyte to the bare material. Alloy exhibited relatively large oscillations attributed to depassivation/repassivation mechanisms, whereas local increments of OCP were observed for MMC during sliding. After sliding, the OCP of both groups immediately increased close to the values observed before sliding as a consequence of repassivation of the worn area [46]. Regarding both bio-functionalized groups, there was no evidence of drop, an almost constant OCP value was recorded during the entire test.

The evolution of COF can be also seen in Fig. 4a. When sliding started, the COF value of Alloy reached values around 0.7 and evolved around this value during sliding with larger oscillations. Regarding MMC samples, once sliding started, COF values were recorded around 0.5 and evolved similar to Alloy till around 750 s and after that, local decrements and increments were observed corresponding to an increments and decrements, respectively, on OCP values. Both bio-functionalized samples presented relatively stable COF values around 0.4 with minor oscillations till the end of sliding.

The representative SEM images of wear tracks, the 2D and 3D wear track profile images together with cross-section SEM images of bio-functionalized groups are also shown in Fig. 4. Alloy presented significantly larger wear track width and more wear damage compared to other groups. Bio-functionalization clearly reduced the wear damage on both Alloy and MMC samples (Fig. 4d and e, respectively). Among bio-functionalized groups, although both groups presented relatively similar wear track width, the MAO-Alloy showed irregular wear track borders.

Worn surface features can be seen in more detail on the representative higher magnification SEM images shown in Fig. 4f–i. Both Alloy and MMC worn surfaces presented parallel sliding grooves and discontinuous tribolayer formation where MMC exhibited smoother surface. Among bio-functionalized samples, distinct worn features clearly observed in Fig. 4h and i. While the worn surface of MAO-Alloy sample exhibited mainly partially damaged MAO layer (removed outer MAO layer), worn MAO-MMC surfaces mainly presented a mixture of smashed outer MAO layer and unaffected zones.

The OM images taken from the wear scars on the alumina balls used as counter-material are presented in Fig. 4j–m. The wear scars on the balls that slid against the untreated samples were much larger than that observed on the balls used to test the MAO treated samples, which is in accordance with the dimensions of the wear tracks. Gross material transfer to the alumina counter-body was observed for Alloy.

Since no well-distinguishable wear loss occurred on bio-functionalized samples, the representative 2D and 3D worn surface profiles are only given for the untreated groups and presented together with the measured total wear volume loss in Fig. 4n and o. The alloy presented drastically deeper and larger wear track in agreement with the wear track SEM images. As can be seen from the profiles, while MMC sample presented rougher wear track, Alloy showed a smooth and uniform wear track. Regarding total wear volume loss values, Alloy presented almost 6 times higher wear volume loss. Cross-sectional SEM image of wear tracks perpendicular to the sliding direction of bio-functionalized samples are given in Fig. 4p and q. A partially damaged MAO layer, after the removal of the outer MAO layer, was observed on worn MAO-Alloy, whereas very less damage was observed on worn MAO-MMC, as in agreement with the top view SEM images of wear tracks.

## 4. Discussion

### 4.1. Microstructure

The size of TiN reinforcement was bigger than the raw TiN powder (1–5 μm) suggesting that the chemical reaction took place during sintering. The XRD and EBSD Kikuchi patterns revealed the reinforced phase as $TiN_{0.3}$, which was uniformly distributed. Also, the top view microstructures (Fig. 1b and c) and the cross-sectional microstructures of MMC (Fig. 2d) showed no evidence of interfacial defects suggesting excellent bonding at the matrix/reinforcement interface resulted from in-situ chemical reaction. It is known that on MMCs, in addition to the direct strengthening by the effect of the reinforcement, indirect strengthening resulted from the alterations on matrix structure such as stain hardening, dislocations and grain refinement is occurred. Consequently, a significant increase was obtained on hardness values from $275 \pm 4$ $HV_{15}$ to $449 \pm 17$ $HV_{15}$, as also previously been reported for 5% vol. TiN reinforced pure Ti [26], thanks to thermodynamic compatibility and contamination-free matrix-reinforcement interface, along with classical composite strengthening mechanisms [47].

MAO is one of the most effective surface modification techniques for the bio-functionalization of valve metals and their alloys due to its simplicity, high efficiency, and low cost [48]. The incorporation of Ca and P bioactive elements were successfully achieved, that are reported to improve the biological behavior of implant materials since they are naturally presented in bones [49]. Also, the created higher surface roughness is known to be suitable for cell adhesion [50]. Moreover, the XRD results showed the formation of anatase and rutile phases in the MAO layer suggesting better osteointegration compared to bare materials [39]. Apart from its thickness, no visible differences on the microstructure of the MAO layer was observed after the incorporation of the reinforcement, while both bio-functionalized groups presented the same Ca/P ratio and crystalline anatase and rutile phases on the MAO layer. Concerning wettability, although both bio-functionalized groups showed the same and drastically lower contact angle ($18 \pm 2$), MMC group ($57 \pm 3$) presented lower values than the values of Alloy ($81 \pm 5$), indicating improvement of hydrophilicity of the surface. The decrement of contact angle with MAO layer formation is mainly due to formation of higher surface porosity and rougher topography [38]. The decrement on contact angle with reinforcement has been also reported for laser

**Table 2**
EEC parameters obtained from EIS data for all groups of samples.

| Samples | $R_{ox}$ (MΩ cm²) | $Q_{ox}$ (×10⁻⁵ F cm⁻² sⁿ⁻¹) | $n_{ox}$ | $Q_{bf}$ (×10⁻⁵ F cm⁻² sⁿ⁻¹) | $n_{bf}$ | $Q_{1/2wall}$ (×10⁻⁵ F cm⁻² sⁿ⁻¹) | $n_{1/2wall}$ | $Q_{wall}$ (×10⁻⁵ F cm⁻² sⁿ⁻¹) | $n_{wall}$ | $\chi^2$ (×10⁻⁴) |
|---|---|---|---|---|---|---|---|---|---|---|
| Alloy | 0.32 ± 0.06 | 3.35 ± 0.46 | 0.91 ± 0.01 | – | – | – | – | – | – | 1.0 ± 0.2 |
| MMC | 0.99 ± 0.57 | 3.20 ± 0.13 | 0.94 ± 0.01 | – | – | – | – | – | – | 1.4 ± 0.3 |
| MAO-Alloy | – | – | – | 3.12 ± 0.06 | 0.71 ± 0.01 | 1.97 ± 0.26 | 0.72 ± 0.01 | 0.17 ± 0.03 | 0.83 ± 0.01 | 1.3 ± 0.2 |
| MAO-MMC | – | – | – | 2.33 ± 0.54 | 0.64 ± 0.04 | 1.52 ± 0.53 | 0.73 ± 0.02 | 0.19 ± 0.03 | 0.82 ± 0.01 | 0.3 ± 0.2 |
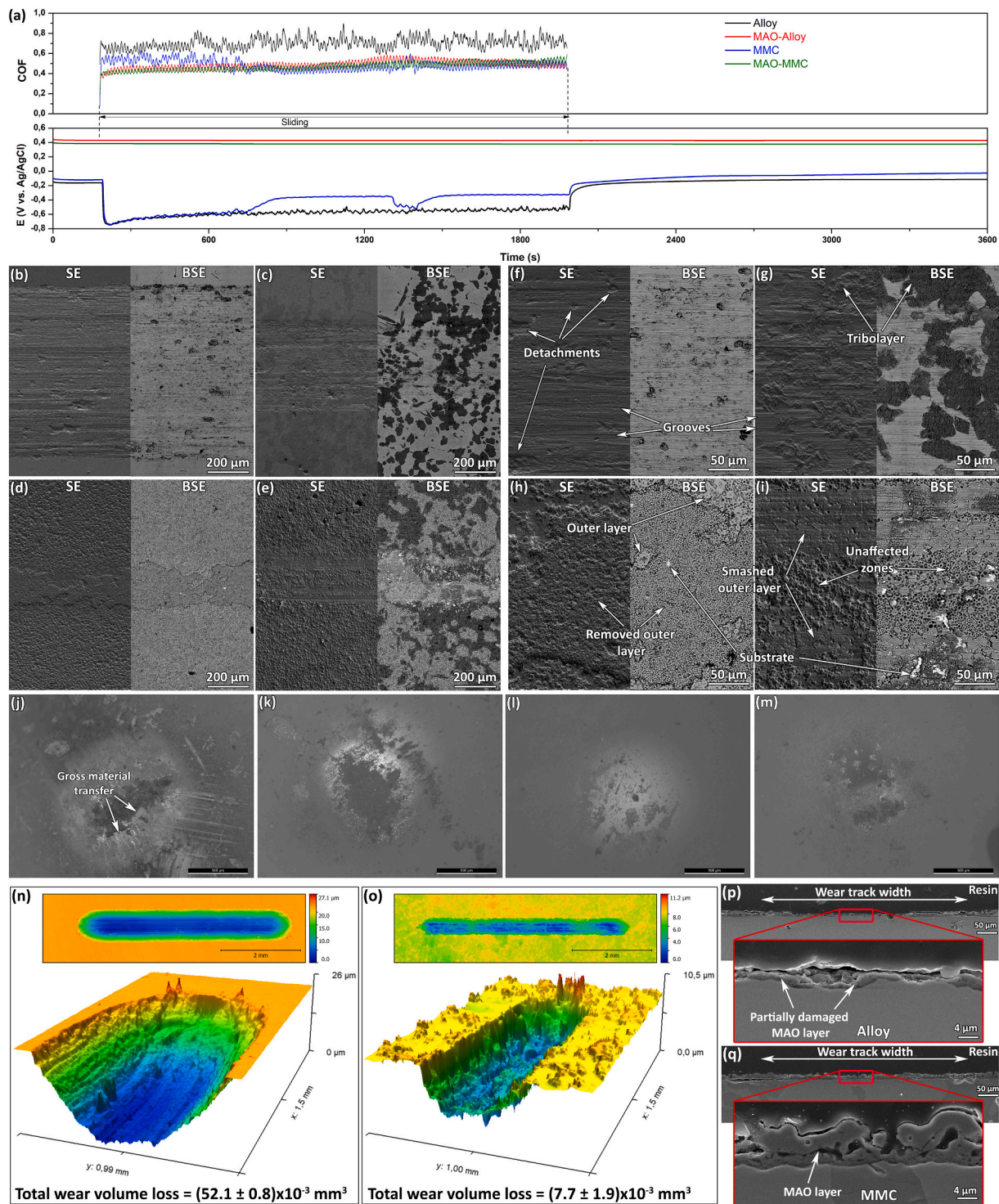
**Fig. 4.** Tribocorrosion behavior: a) The representative evolution of OCP before, during, and after sliding, together with the evolution of COF under sliding; lower magnification SE and BSE SEM images of wear tracks for b) Alloy, c) MMC, d) MAO-Alloy, and e) MAO-MMC; higher magnification SE and BSE images of worn surfaces for f) Alloy, g) MMC, h) MAO-Alloy, and i) MAO-MMC; wear scar OM images of counter material for j) Alloy, k) MMC, l) MAO-Alloy, and m) MAO-MMC; representative 2D and 3D (taken from the border of the wear tracks) wear track images, and measured total wear volume loss for n) Alloy and o) MMC; cross-section SEM images of wear tracks perpendicular to the sliding direction for (p) MAO-Alloy and (q) MAO-MMC.

processed TiN reinforced Ti-6Al-4V due to their higher surface energy as compared to the unreinforced alloy [51]. Hydrophilic surfaces are more prone to adhesion of proteins, molecules, cells, and tissue interactions, and improving osteointegration rate [52]. Therefore, the bio-functionalization may improve bioactivity in a biological environment by transforming the surfaces from hydrophobic to hydrophilic together

with other factors such as Ca/Pa ratio, surface roughness, and crystal structure, as discussed above.

### 4.2. Corrosion behavior

The defects at matrix/reinforcement interface such as cracks,

porosity, discontinuities, and gaps are known as a determining factor on the corrosion behavior of MMCs, may be resulted in localized corrosion and galvanic coupling between the matrix and the reinforcement [32,33,53,54]. Based on the results, a clean and compatible interface was obtained for MMC samples resulted from the chemical reaction. Also, the corrosion results did not suggest any localized corrosion and galvanic coupling between the matrix and the reinforcement. Thus, the same EEC was used for both untreated groups that consider a native oxide film was formed on the surface of the samples exposed to PBS solution without any discontinuities on the matrix/reinforcement interface. As can be seen in Table 2, both Alloy and MMC samples showed similar $E_{OCP}$, $E_{(i=0)}$, $i_{pass}$ and $Q_{ox}$ values, but the MMC presented higher $R_{ox}$ values suggesting better corrosion resistance, which is in accordance with its higher $|Z|_{f \to 0}$ and higher phase angles at middle and lower frequency. Also, since surface heterogeneities influence the $n$ values, lower $n_{ox}$ values obtained for Alloy points higher surface heterogeneities resulted from its porosity as observed in Fig. 1a. This better corrosion behavior of MMC may be explained by the contribution of the $TiN_{0.3}$ reinforcing phase acting as inert physical barrier, similar to several MMC systems reported in the literature [55].

It is well reported that MAO treatment improves the corrosion behavior of Ti and its alloys [34,35,56,57]. Both bio-functionalized groups presented significantly higher $E_{OCP}$ and $E_{(i=0)}$, and lower $i_{pass}$ values compared to the untreated groups indicating their lower tendency to corrosion and corrosion rate in PBS solution. Regarding EIS, the same EEC had proposed before by some of the present authors to fit the results of MAO treated cp-Ti under the same conditions [35,58]. According to the EEC parameters given in Table 2, there was no significant difference between $Q$ and $n$ values of both bio-functionalized groups. The observed lower $n$ values of bio-functionalized groups compared to the $n_{ox}$ may be due to increased roughness and heterogeneities. The bio-functionalized groups presented similar $n$ values except for $n_{bf}$, that might be due to chemical heterogeneities on barrier film formed on MAO-MMC sample. The lower $Q_{wall}$ values compared with their $Q_{1/2wall}$ results from the higher thickness of the pores walls, since the thickness is inversely proportional to capacitance. Also, the $Q_{bf}$ values of bio-functionalized groups were lower than the $Q_{ox}$ values of untreated groups suggesting improvement of corrosion behavior with MAO treatment.

## 4.3. Tribocorrosion behavior

The suggested tribocorrosion mechanisms are schematically illustrated in Fig. 5. The observed larger and unstable COF values with severe wear damage of Alloy resulted in higher wear volume loss revealed a dominantly adhesive wear mechanism as also evidenced on gross transfer of the substrate to the counter material slid against Alloy (Fig. 4j). Also, the parallel grooves on wear track of Alloy suggested abrasive wear mechanism, which can be explained by the ploughing action of the transferred material on the counter body. Similar dominant abrasive/adhesive mechanisms were reported for different β type Ti alloys under different testing conditions [8,10,11,59,60].

Similar wear mechanism was also observed for MMC, but with less visible wear damage and drastically lower wear volume loss, mainly due to the load-carrying effect of harder reinforcement phase, together with the contribution of the indirect strengthening resulted in the drastically increased hardness. Moreover, the formation of a tribolayer may also play a role for lower wear volume loss (Fig. 4g). The formation of tribolayer particularly observed on the reinforcement phase that may be explained by its the higher hardness, since, as reported by Cvijovic et al. [8], the harder material is able to hold a thicker oxide layer more uniformly as compared to a softer material. Likewise, β-Ti matrix does not have sufficient ability to hold an oxide patch during sliding due to its low plastic shear resistance [9]. As can be seen from Fig. 4, while MMC presented lower overall COF values, it presented relatively similar OCP and COF evolution up to around 750 s. After that time, the gradual increment on the OCP and decrement on the COF, followed by a relatively stable behavior suggested formation of a tribolayer. As observed in Fig. 4g, this tribolayer was in a discontinuous form. Also, this tribolayer might get thicker with sliding time, and due to its physical protection role, it may cause a local increment on OCP values. However, after reaching a certain thickness, it might be swept away by the counter body. Therefore, the repetitive thickening and breaking of this tribolayer can induce the decrements and increments both in OCP and COF values. Similar mechanisms were reported by Silva et al. [33] for Ti-TiB-TiN$_x$ hybrid composite on reciprocating sliding under 1 N of normal load and 1 Hz of frequency in 9 g/l NaCl solution, where a continuous and compacted tribolayer played a dominant role on the wear mechanism.

Bio-functionalization drastically improved the tribocorrosion
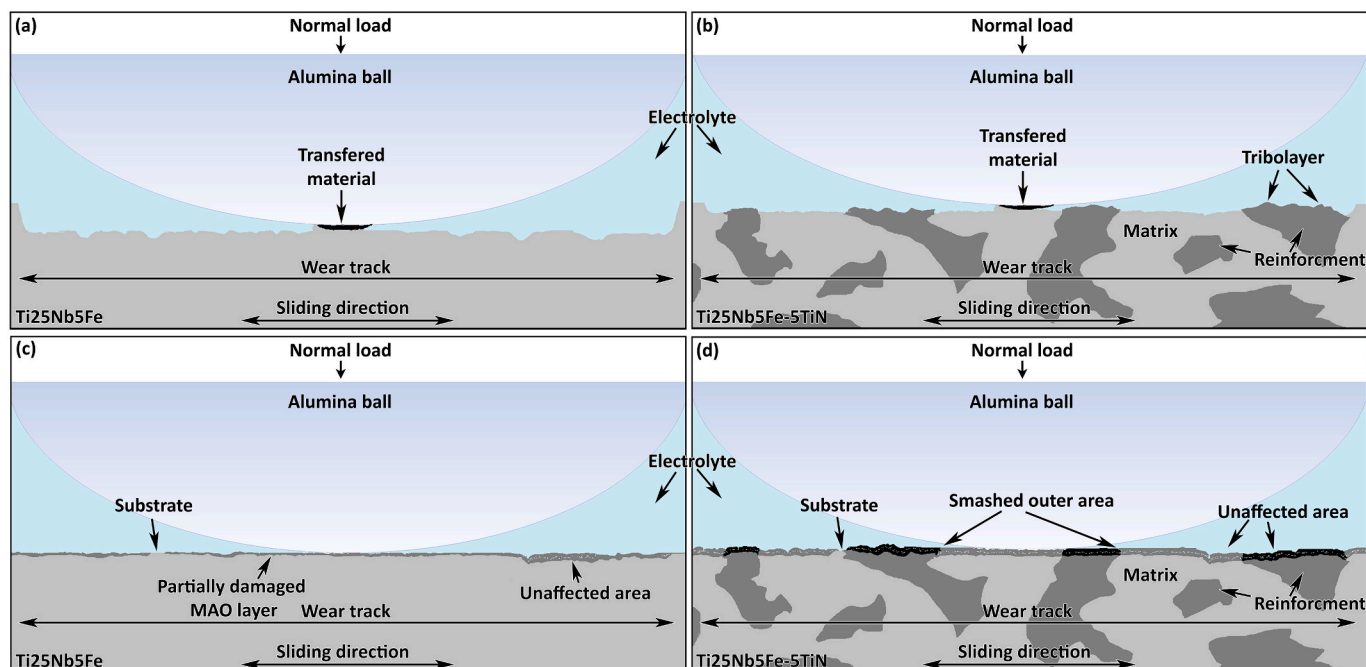


**Fig. 5.** Schematic illustrations of tribocorrosion mechanisms for a) Alloy, b) MMC, c) MAO-Alloy, and d) MAO-MMC samples.

behavior of both alloy and MMC as evidenced by nobler OCP values, lower and more stable COF values, and less visible damage on the surfaces. The tribocorrosion mechanisms of the MAO layers formed on cp-Ti (grade 2) already reported in the literature [34,36,61]. Oliveira et al. [34] studied a MAO layer composed of an amorphous outer layer followed by a gradient rutile to anatase structure formed due to a very high cooling rate during MAO treatment. As soon as sliding started, this amorphous layer easily worn out due to high contact pressure resulted from its high surface roughness. The rutile-anatase crystalline barrier layer played a main protective role against wear due to better mechanical behavior of the crystalline phases, especially the higher hardness of the rutile phase [36]. The observed irregular shape of wear track in the case of MAO-Alloy was due to the detachment of the outer porous layer during sliding. While small local damages of the MAO layer were observed on the worn surface of the Alloy, as can be seen more clearly in Fig. 4p, a partially damaged MAO layer was still survived against the counter body. In the case of MAO-MMC samples, since they presented relatively less damage of the MAO layer, most of the wear track composed of unaffected (intact) surfaces and/or smashed outer MAO layer. The better wear behavior of MAO-MMC samples compared to the MAO-Alloy samples may be explained by the pillar effect of the $TiN_{0.3}$ reinforcing phases under the $TiO_2$ MAO surface. The MAO layer formed on hard $TiN_{0.3}$ phase seems to carry efficiently the applied load, and thus its wear track presented less overall damage (Fig. 4q).

This is a novel concept for the bio-functionalization of β type Ti alloy matrix composites through MAO treatment for load-bearing implants. Although the MAO-MMC group presented promising behavior under the studied conditions, several studies need to be performed such as a detailed mechanical characterization (especially Young's modulus), the investigation of corrosion, and tribocorrosion behavior in more complex electrolytes, and finally the analysis of biological behavior in vitro and in vivo. Finally, in order to minimize the increase on Young's modulus after the addition of TiN particles, instead of bulk MMCs, functionally graded metal matrix composite concept can be considered.

## 5. Conclusion

The β type Ti-25Nb-5Fe alloy was reinforced with 5 vol% TiN particles and both alloy and composites were bio-functionalized with incorporation Ca and P through MAO treatment. The Alloy and MMC showed similar corrosion behavior and their corrosion behavior was significantly improved by the bio-functionalization treatment, mostly due to the formation of thicker oxide layer compared to their passive film. While the tribocorrosion behavior of Alloy improved with TiN reinforcement resulted from drastically improved hardness and microstructure, it was further improved by the bio-functionalization treatment due to obtaining a thick rutile-anatase $TiO_2$ layer. The MAO layer formed on the composites stayed mostly intact after tribocorrosion due to the pillar effect given by the reinforcements.

## CRediT authorship contribution statement

**Ihsan Çaha:** Conceptualization, Methodology, Formal analysis, Investigation, Data curation, Writing – original draft, Visualization. **Alexandra C. Alves:** Conceptualization, Formal analysis, Writing – review & editing. **Caterina Chirico:** Methodology. **Ana Maria Pinto:** Resources, Methodology. **Sophia Tsipas:** Methodology. **Elena Gordo:** Methodology, Writing – review & editing. **Fatih Toptan:** Conceptualization, Formal analysis, Visualization, Resources, Writing – review & editing, Supervision, Project administration, Funding acquisition.

## Declaration of competing interest

The authors declare that they have no known competing financial interests or personal relationships that could have appeared to influence the work reported in this paper.

## References

[1] M. Niinomi, M. Nakai, J. Hieda, Development of new metallic alloys for biomedical applications, Acta Biomater. 8 (2012) 3888–3903, https://doi.org/10.1016/j.actbio.2012.06.037.

[2] M. Geetha, A.K. Singh, R. Asokamani, A.K. Gogia, Ti based biomaterials, the ultimate choice for orthopaedic implants - a review, Prog, Mater. Sci. 54 (2009) 397–425, https://doi.org/10.1016/j.pmatsci.2008.06.004.

[3] Y. Bai, Y. Deng, Y. Zheng, Y. Li, R. Zhang, Y. Lv, Q. Zhao, S. Wei, Characterization, corrosion behavior, cellular response and in vivo bone tissue compatibility of titanium-niobium alloy with low Young's modulus, Mater. Sci. Eng. C 59 (2016) 565–576, https://doi.org/10.1016/j.msec.2015.10.062.

[4] A.H. Glassman, J.D. Bobyn, M. Tanzer, New femoral designs: do they influence stress shielding?, Clin, Orthop. Relat. Res. 453 (2006) 64–74, https://journals.lww.com/clinorthop/Fulltext/2006/12000/New_Femoral_Designs__Do_They_Influence_Stress.12.aspx.

[5] M. Niinomi, Recent metallic materials for biomedical applications, Metall, Mater. Trans. A. 33 (2002) 477–486, https://doi.org/10.1007/s11661-002-0109-2.

[6] E. Eisenbarth, D. Velten, M. Müller, R. Thull, J. Breme, Biocompatibility of β-stabilizing elements of titanium alloys, Biomaterials. 25 (2004) 5705–5713, https://doi.org/10.1016/j.biomaterials.2004.01.021.

[7] P.R. Walker, J. LeBlanc, M. Sikorska, Effects of aluminum and other cations on the structure of brain and liver chromatin, Biochemistry. 28 (1989) 3911–3915, https://doi.org/10.1021/bi00435a043.

[8] Z. Cvijovic, S. Mitrovic, V. Panic, Wear and corrosion behaviour of Ti–13Nb–13Zr and Ti–6Al–4V alloys in simulated physiological solution, Corros, Sci. 53 (2011) 796–808, https://doi.org/10.1016/j.corsci.2010.11.014.

[9] Y.S. Lee, M. Niinomi, M. Nakai, K. Narita, K. Cho, Predominant factor determining wear properties of β-type and (α+β)-type titanium alloys in metal-to-metal contact for biomedical applications, J. Mech. Behav. Biomed. Mater. 41 (2015) 208–220, https://doi.org/10.1016/j.jmbbm.2014.10.005.

[10] X. Yang, C.R. Hutchinson, Corrosion-wear of β-Ti alloy alloy TMZF (Ti-12Mo-6Zr-2Fe) in simulated body fluid, Acta Biomater. 42 (2016) 429–439, https://doi.org/10.1016/j.actbio.2016.07.008.

[11] I. Çaha, A.C. Alves, P.A.B. Kuroda, C.R. Grandini, A.M.P. Pinto, L.A. Rocha, F. Toptan, Degradation behaviour of Ti-Nb alloys: corrosion behavior through 21 days of immersion and tribocorrosion behavior against alumina, Corros, Sci. 167 (2020), 108488, https://doi.org/10.1016/j.corsci.2020.108488.

[12] D. Bitar, Biological response to prosthetic debris, World J. Orthop. 6 (2015) 172, https://doi.org/10.5312/wjo.v6.i2.172.

[13] F. Galliano, E. Galvanetto, S. Mischler, D. Landolt, Tribocorrosion behavior of plasma nitrided Ti-6Al-4V alloy in neutral NaCl solution, Surf, Coatings Technol. 145 (2001) 121–131, https://doi.org/10.1016/S0257-8972(01)01309-3.

[14] D. Nolan, S.W. Huang, V. Leskovsek, S. Braun, Sliding wear of titanium nitride thin films deposited on Ti-6Al-4V alloy by PVD and plasma nitriding processes, Surf, Coatings Technol. 200 (2006) 5698–5705, https://doi.org/10.1016/j.surfcoat.2005.08.110.

[15] Ł. Łapaj, J. Wendland, J. Markuszewski, A. Mróz, T. Wiśniewski, Retrieval analysis of titanium nitride (TiN) coated prosthetic femoral heads articulating with polyethylene, J. Mech. Behav. Biomed. Mater. 55 (2016) 127–139, https://doi.org/10.1016/j.jmbbm.2015.10.012.

[16] A. Vadiraj, M. Kamaraj, Effect of surface treatments on fretting fatigue damage of biomedical titanium alloys, Tribol. Int. 40 (2007) 82–88, https://doi.org/10.1016/j.triboint.2006.02.064.

[17] A. Samanta, M. Bhattacharya, I. Ratha, H. Chakraborty, S. Datta, J. Ghosh, S. Bysakh, M. Sreemany, R. Rane, A. Joseph, S. Mukherjee, B. Kundu, M. Das, A. K. Mukhopadhyay, Nano- and micro-tribological behaviours of plasma nitrided Ti6Al4V alloys, J. Mech. Behav. Biomed. Mater. 77 (2018) 267–294, https://doi.org/10.1016/j.jmbbm.2017.09.013.

[18] W. Cui, G. Qin, J. Duan, H. Wang, A graded nano-TiN coating on biomedical Ti alloy: low friction coefficient, good bonding and biocompatibility, Mater. Sci. Eng. C. 71 (2017) 520–528, https://doi.org/10.1016/j.msec.2016.10.033.

[19] E. Santecchia, A.M.S. Hamouda, F. Musharavati, E. Zalnezhad, M. Cabibbo, S. Spigarelli, Wear resistance investigation of titanium nitride-based coatings, Ceram. Int. 41 (2015) 10349–10379, https://doi.org/10.1016/j.ceramint.2015.04.152.

[20] I. Çaha, A.C. Alves, L.J. Affonço, P.N. Lisboa-Filho, J.H.D. da Silva, L.A. Rocha, A. M.P. Pinto, F. Toptan, Corrosion and tribocorrosion behaviour of titanium nitride

thin films grown on titanium under different deposition times, Surf, Coatings Technol. 374 (2019) 878–888, https://doi.org/10.1016/j.surfcoat.2019.06.073.

[21] T.M. Manhabosco, S.M. Tamborim, C.B. dos Santos, I.L. Müller, Tribological, electrochemical and tribo-electrochemical characterization of bare and nitrided Ti6Al4V in simulated body fluid solution, Corros, Sci. 53 (2011) 1786–1793, https://doi.org/10.1016/j.corsci.2011.01.057.

[22] M. Annunziata, A. Oliva, M.A. Basile, M. Giordano, N. Mazzola, A. Rizzo, A. Lanza, L. Guida, The effects of titanium nitride-coating on the topographic and biological features of TPS implant surfaces, J. Dent. 39 (2011) 720–728, https://doi.org/10.1016/j.jdent.2011.08.003.

[23] M.T. Mathew, P. Srinivasa Pai, R. Pourzal, A. Fischer, M.A. Wimmer, Significance of tribocorrosion in biomedical applications: overview and current status, Adv, Tribol. (2009) 12, https://doi.org/10.1155/2009/250986.

[24] R.J.K. Wood, Tribo-corrosion of coatings: a review, J. Phys. D. Appl. Phys. 40 (2007) 5502–5521, https://doi.org/10.1088/0022-3727/40/18/S10.

[25] M. Rosso, Ceramic and metal matrix composites: routes and properties, J. Mater. Process. Technol. 175 (2006) 364–375, https://doi.org/10.1016/j.jmatprotec.2005.04.038.

[26] F. Romero, V. Amigó, M.D. Salvador, A. Vicente, Interactions in titanium matrix composites reinforced by titanium compounds by conventional PM route, Mater. Sci. Forum 534–536 (2007) 817–820. doi:https://doi.org/10.4028/www.scientific.net/msf.534-536.817.

[27] M.E. Maja, O.E. Falodun, B.A. Obadele, S.R. Oke, P.A. Olubambi, Nanoindentation studies on TiN nanoceramic reinforced Ti–6Al–4V matrix composite, Ceram. Int. 44 (2018) 4419–4425, https://doi.org/10.1016/j.ceramint.2017.12.042.

[28] O.E. Falodun, B.A. Obadele, S.R. Oke, M.E. Maja, P.A. Olubambi, Effect of sintering parameters on densification and microstructural evolution of nano-sized titanium nitride reinforced titanium alloys, J. Alloys Compd. 736 (2018) 202–210, https://doi.org/10.1016/j.jallcom.2017.11.140.

[29] S. Kundu, M. Hussain, V. Kumar, S. Kumar, A.K. Das, Direct metal laser sintering of TiN reinforced Ti6Al4V alloy based metal matrix composite: fabrication and characterization, Int. J. Adv. Manuf. Technol. 97 (2018) 2635–2646, https://doi.org/10.1007/s00170-018-2159-7.

[30] A.M. Ribeiro, A.C. Alves, F.S. Silva, F. Toptan, Electrochemical characterization of hot pressed CoCrMo–HAP biocomposite in a physiological solution, Mater. Corros. 66 (2015) 790–795, https://doi.org/10.1002/maco.201407885.

[31] F. Toptan, A. Rego, A.C. Alves, A. Guedes, Corrosion and tribocorrosion behavior of Ti–B4C composite intended for orthopaedic implants, J. Mech. Behav. Biomed. Mater. 61 (2016) 152–163, https://doi.org/10.1016/j.jmbbm.2016.01.024.

[32] B. Bobić, S. Mitrovic, M. Babic, I. Bobić, Corrosion of aluminium and zinc-aluminium alloys based metal-matrix composites, Tribol, Ind. 31 (2009) 44–53. https://www.scopus.com/inward/record.uri?eid=2-s2.0-73949137681&partnerID=40&md5=e6b16abb35b092f2435644231ff63e75.

[33] J.I. Silva, A.C. Alves, A.M. Pinto, F. Toptan, Corrosion and tribocorrosion behavior of Ti–TiB−TiNx in-situ hybrid composite synthesized by reactive hot pressing, J. Mech. Behav. Biomed. Mater. 74 (2017) 195–203, https://doi.org/10.1016/j.jmbbm.2017.05.041.

[34] F.G. Oliveira, A.R. Ribeiro, G. Perez, B.S. Archanjo, C.P. Gouvea, J.R. Araújo, A.P. C. Campos, A. Kuznetsov, C.M. Almeida, M.M. Maru, C.A. Achete, P. Ponthiaux, J. Celis, L.A. Rocha, Understanding growth mechanisms and tribocorrosion behaviour of porous TiO2 anodic films containing calcium, phosphorous and magnesium, Appl. Surf. Sci. 341 (2015) 1–12, https://doi.org/10.1016/j.apsusc.2015.02.163.

[35] A.C. Alves, F. Wenger, P. Ponthiaux, J.P. Celis, A.M. Pinto, L.A. Rocha, J.C. S. Fernandes, Corrosion mechanisms in titanium oxide-based films produced by anodic treatment, Electrochim. Acta 234 (2017) 16–27, https://doi.org/10.1016/j.electacta.2017.03.011.

[36] A.C. Alves, F. Oliveira, F. Wenger, P. Ponthiaux, J.-P. Celis, L.A. Rocha, Tribocorrosion behaviour of anodic treated titanium surfaces intended for dental implants, J. Phys. D. Appl. Phys. 46 (2013) 404001–9. doi:https://doi.org/10.1088/0022-3727/46/40/404001.

[37] D.R.N. Correa, L.A. Rocha, A.R. Ribeiro, S. Gemini-Piperni, B.S. Archanjo, C. A. Achete, J. Werckmann, C.R.M. Afonso, M. Shimabukuro, H. Doi, Y. Tsutsumi, T. Hanawa, Growth mechanisms of Ca- and P-rich MAO films in Ti-15Zr-xMo alloys for osseointegrative implants, Surf, Coatings Technol. 344 (2018) 373–382, https://doi.org/10.1016/j.surfcoat.2018.02.099.

[38] M.B. Sedelnikova, E.G. Komarova, Y.P. Sharkeev, A.V. Ugodchikova, L. S. Mushtovatova, M.R. Karpova, V.V. Sheikin, L.S. Litvinova, I.A. Khlusov, Zn-, Cu- or Ag-incorporated micro-arc coatings on titanium alloys: properties and behavior in synthetic biological media, Surf, Coatings Technol. 369 (2019) 52–68, https://doi.org/10.1016/j.surfcoat.2019.04.021.

[39] H. Te Chen, C.J. Chung, T.C. Yang, C.H. Tang, J.L. He, Microscopic observations of osteoblast growth on micro-arc oxidized β titanium, Appl. Surf. Sci. 266 (2013) 73–80, https://doi.org/10.1016/j.apsusc.2012.11.087.

[40] L. Zhao, Y. Wei, J. Li, Y. Han, R. Ye, Y. Zhang, Initial osteoblast functions on Ti-5Zr-3Sn-5Mo-15Nb titanium alloy surfaces modified by microarc oxidation, J. Biomed. Mater. Res. - Part A. 92 (2010) 432–440, https://doi.org/10.1002/jbm.a.32348.

[41] S. Yu, Z. Yu, G. Wang, J. Han, X. Ma, M.S. Dargusch, Biocompatibility and osteoconduction of active porous calcium-phosphate films on a novel Ti-3Zr-2Sn-3Mo-25Nb biomedical alloy, Colloids Surfaces B Biointerfaces. 85 (2011) 103–115, https://doi.org/10.1016/j.colsurfb.2011.02.025.

[42] S.J. CLi, C.Y. Zheng, J. Fu, Z. Guo, Y.L. Hao, R. Yang, Z.X. Guo, Synthesis of a porous oxide layer on a multifunctional biomedical titanium by micro-arc oxidation, Mater. Sci. Eng. C. 29 (2009) 1923–1934, https://doi.org/10.1016/j.msec.2009.03.004.

[43] S. Yu, Z.T. Yu, G. Wang, J.Y. Han, X.Q. Ma, M.S. Dargusch, Preparation and osteoinduction of active micro-arc oxidation films on Ti-3Zr-2Sn-3Mo-25Nb alloy, Trans. Nonferrous Met. Soc. China (English Ed. 21 (2011) 573–580. doi:https://doi.org/10.1016/S1003-6326(11)60753-X.

[44] M.B. Sedelnikova, Y.P. Sharkeev, E.G. Komarova, I.A. Khlusov, V.V. Chebodaeva, Structure and properties of the wollastonite–calcium phosphate coatings deposited on titanium and titanium–niobium alloy using microarc oxidation method, Surf, Coatings Technol. 307 (2016) 1274–1283, https://doi.org/10.1016/j.surfcoat.2016.08.062.

[45] A. Kazek-Kęsik, M. Krok-Borkowicz, G. Dercz, A. Donesz-Sikorska, E. Pamuła, W. Simka, Multilayer coatings formed on titanium alloy surfaces by plasma electrolytic oxidation-electrophoretic deposition methods, Electrochim. Acta 204 (2016) 294–306, https://doi.org/10.1016/j.electacta.2016.02.193.

[46] T. Hanawa, K. Asami, K. Asaoka, Repassivation of titanium and surface oxide film regenerated in simulated bioliquid, J. Biomed. Mater. Res. 40 (1998) 530–538, https://doi.org/10.1002/(SICI)1097-4636(19980615)40:4<530::AID-JBM3>3.0.CO;2-G.

[47] W.J. Lu, D. Zhang, R.J. Wu, H. Mori, Solidification paths and reinforcement morphologies in melt-processed (TiB + TiC)/Ti in situ composites, Metall, Mater. Trans. A Phys. Metall. Mater. Sci. 33 (2002) 3055–3063, https://doi.org/10.1007/s11661-002-0290-3.

[48] Y. Wang, H. Yu, C. Chen, Z. Zhao, Review of the biocompatibility of micro-arc oxidation coated titanium alloys, Mater. Des. 85 (2015) 640–652, https://doi.org/10.1016/j.matdes.2015.07.086.

[49] C.E. Tanase, M. Golozar, S.M. Best, R.A. Brooks, Cell response to plasma electrolytic oxidation surface-modified low-modulus β-type titanium alloys, Colloids Surfaces B Biointerfaces. 176 (2019) 176–184, https://doi.org/10.1016/j.colsurfb.2018.12.064.

[50] J.I. Rosales-Leal, M.A. Rodríguez-Valverde, G. Mazzaglia, P.J. Ramón-Torregrosa, L. Díaz-Rodríguez, O. García-Martínez, M. Vallecillo-Capilla, C. Ruiz, M. A. Cabrerizo-Vílchez, Effect of roughness, wettability and morphology of engineered titanium surfaces on osteoblast-like cell adhesion, Colloids Surfaces A Physicochem, Eng. Asp. 365 (2010) 222–229, https://doi.org/10.1016/j.colsurfa.2009.12.017.

[51] V.K. Balla, A. Bhat, S. Bose, A. Bandyopadhyay, Laser processed TiN reinforced Ti6Al4V composite coatings, J. Mech. Behav. Biomed. Mater. 6 (2012) 9–20, https://doi.org/10.1016/j.jmbbm.2011.09.007.

[52] R.A. Gittens, L. Scheideler, F. Rupp, S.L. Hyzy, J. Geis-Gerstorfer, Z. Schwartz, B. D. Boyan, A review on the wettability of dental implant surfaces II: biological and clinical aspects, Acta Biomater. 10 (2014) 2907–2918, https://doi.org/10.1016/j.actbio.2014.03.032.

[53] F. Toptan, L.A. Rocha, Tribocorrosion in metal matrix composites, Mater. Sci. Eng. Concepts, Methodol. Tools, Appl. 2–3 (2017) 825–844, https://doi.org/10.4018/978-1-5225-1798-6.ch032.

[54] L.H. Hihara, R.M. Latanision, Corrosion of metal matrix composites, Int, Mater. Rev. 39 (1994) 245–264, https://doi.org/10.1179/imr.1994.39.6.245.

[55] K.H.W. Seah, M. Krishna, V.T. Vijayalakshmi, J. Uchil, Corrosion behaviour of garnet particulate reinforced LM13 Al alloy MMCs, Corros, Sci. 44 (2002) 917–925, https://doi.org/10.1016/S0010-938X(01)00099-3.

[56] A. Kazek-Kęsik, M. Krok-Borkowicz, E. Pamuła, W. Simka, Electrochemical and biological characterization of coatings formed on Ti-15Mo alloy by plasma electrolytic oxidation, Mater. Sci. Eng. C. 43 (2014) 172–181, https://doi.org/10.1016/j.msec.2014.07.021.

[57] C.F. Liu, T.H. Lee, J.F. Liu, W.T. Hou, S.J. Li, Y.L. Hao, H. Pan, H.H. Huang, A unique hybrid-structured surface produced by rapid electrochemical anodization enhances bio-corrosion resistance and bone cell responses of β-type Ti-24Nb-4Zr-8Sn alloy, Sci, Rep. 8 (2018) 1–14, https://doi.org/10.1038/s41598-018-24590-x.

[58] A.C. Alves, A.I. Costa, F. Toptan, J.L. Alves, I. Leonor, E. Ribeiro, R.L. Reis, A.M. P. Pinto, J.C.S. Fernandes, Effect of bio-functional MAO layers on the electrochemical behaviour of highly porous Ti, Surf, Coatings Technol. 386 (2020), 125487, https://doi.org/10.1016/j.surfcoat.2020.125487.

[59] I. Çaha, A. Alves, C. Chirico, A. Pinto, S. Tsipas, E. Gordo, F. Toptan, Corrosion and tribocorrosion behavior of Ti-40Nb and Ti-25Nb-5Fe alloys processed by powder metallurgy, Metall, Mater. Trans. A Phys. Metall. Mater. Sci. 51 (2020) 3256–3267, https://doi.org/10.1007/s11661-020-05757-6.

[60] Y. Lee, M. Niinomi, M. Nakai, K. Narita, K. Cho, Differences in wear behaviors at sliding contacts for β-type and (α + β)-type titanium alloys in Ringer's solution and air, Mater, Trans. 56 (2015) 317–326.

[61] A.F. Yetim, Investigation of wear behavior of titanium oxide films, produced by anodic oxidation, on commercially pure titanium in vacuum conditions, Surf, Coatings Technol. 205 (2010) 1757–1763, https://doi.org/10.1016/j.surfcoat.2010.08.079.